Supporting information for: "Monitoring Electron–Phonon Interactions in Lead-Halide Perovskites Using Time-Resolved THz Spectroscopy"

Daming Zhao,[†] Hongwei Hu,[‡] Reinhard Haselsberger,[†] Rudolph A. Marcus,[†,⊥] Maria-Elisabeth Michel-Beyerle,[†] Yeng Ming Lam,[‡] Jian-Xin Zhu,[¶] Chan La-o-vorakiat,[*,§,#] Matthew C. Beard,[*,‖] and Elbert E. M. Chia[*,†]

†*Division of Physics and Applied Physics, School of Physical and Mathematical Sciences, Nanyang Technological University, 637371 Singapore*

‡*School of Materials Science and Engineering, Nanyang Technological University, 639798 Singapore*

¶*Theoretical Division and Center for Integrated Nanotechnologies, Los Alamos National Laboratory, Los Alamos, New Mexico 87545, United States*

§*Nanoscience and Nanotechnology Graduate Program, Faculty of Science, King Mongkut's University of Technology Thonburi (KMUTT), Bangkok 10140 Thailand*

‖*Chemistry and Nanoscience Science Center, National Renewable Energy Laboratory, Golden, Colorado 80401, United States*

⊥*Noyes Laboratory, California Institute of Technology, Pasadena, California 91125, United States*

#*Theoretical and Computational Science Center (TaCS), KMUTT, Bangkok 10140 Thailand*

E-mail: chan.laovorakiat@gmail.com; Matt.Beard@nrel.gov; elbertchia@ntu.edu.sg

S1. Dielectric function and Loss function analysis

To accurately identify both transverse-optical (TO) and longitudinal-optical (LO) phonon frequencies, we employ another THz spectrometer (TPS 3000 by Teraview), with a larger signal-to-noise ratio and frequency range (0.3–2.5 THz), to measure a new FCPIB sample grown from the same batch as the one in the main text.

From the measurements of the time-domain transmitted electric fields through the sample (FCPIB film on z-cut quartz substrate) $E_{sam}(t)$ and through the reference (bare z-cut quartz substrate) $E_{ref}(t)$. We calculate the complex electric field in frequency domain for the sample $\widetilde{E}_{sam}(\omega)$ and the reference $\widetilde{E}_{ref}(\omega)$, respectively, to obtain the transmission coefficient $\widetilde{T}(\omega) = \widetilde{E}_{sam}(\omega)/\widetilde{E}_{ref}(\omega)$. We then extract complex refractive indexes $[\tilde{n}(\omega) = n(\omega) + i\kappa(\omega)]$ from $\widetilde{T}(\omega)$ by numerically solving the equation[S1]

$$\widetilde{T}(\omega) = \frac{2\tilde{n}(\tilde{n}_{sub}+1)exp[i\omega d(\tilde{n}-1)/c]exp[-i\omega\Delta L(\tilde{n}_{sub}-1)/c]}{(1+\tilde{n})(\tilde{n}+\tilde{n}_{sub})+(\tilde{n}-1)(\tilde{n}_{sub}-\tilde{n})exp[2i\omega d\tilde{n}/c]}, \tag{S1}$$

where $\tilde{n}_{sub}$ is the refractive index of z-cut quartz substrate, d is the film thickness, c is the speed of light in vacuum and ΔL is the difference in thickness of the sample and reference substrates. The refractive index extraction using Eq. S1 yields exact solutions without resorting to the thin-film approximation.[S2] Through the relation $\tilde{\epsilon}(\omega) = \tilde{n}^2(\omega)$, the 15 K FCPIB complex dielectric function $\tilde{\epsilon}(\omega) = \epsilon_1(\omega) + i\epsilon_2(\omega)$ is calculated and shown in Fig. S1A below. We take ϵ_1 at 0.3 THz as our low-frequency dielectric function ϵ_{static} ($\sim$50). We model the dielectric function $\tilde{\epsilon}(\omega)$ with two Lorentz oscillators,

$$\tilde{\epsilon}(\omega) = \epsilon_\infty + \sum_{m=1}^{2} \frac{\omega_{p,m}^2}{\omega_{TO,m}^2 - \omega^2 - i\omega\gamma_m}, \tag{S2}$$

where $\omega_{p,m}$, $\omega_{TO,m}$, γ_m and ϵ_∞ are the oscillator strength, TO-phonon frequency, linewidth of the m^{th} oscillator and the high-frequency dielectric constant, respectively, and simultaneously fit $\epsilon_1(\omega)$ and $\epsilon_2(\omega)$ (solid lines in Fig. S1A). Peaks in $\epsilon_2(\omega)$ indicate the locations of the TO-

phonon modes. We obtain $\frac{\omega_{TO,1}}{2\pi}$ = 0.88 THz (3.6 meV), $\frac{\omega_{TO,2}}{2\pi}$ = 1.76 THz (7.3 meV) and $\epsilon_\infty = 6.8$ from the fit.

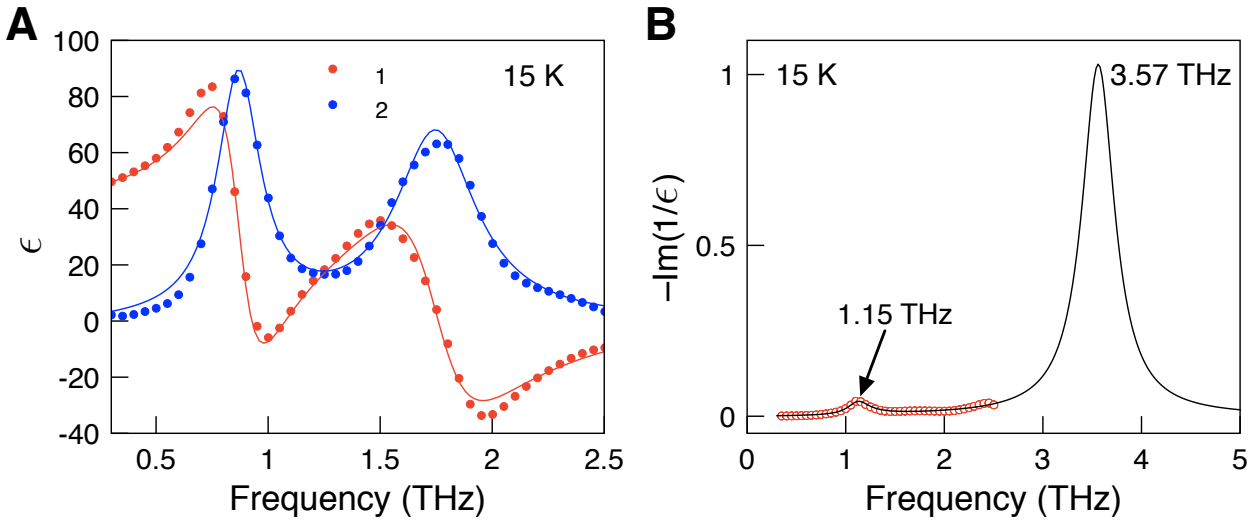

Figure S1: **Dielectric function and loss function analysis.** (A) Complex dielectric function data (dots) and the fit (lines). (B) Measured (red circles) and extrapolated (black line) loss function $-\mathrm{Im}[1/\tilde{\epsilon}(\omega)]$ based on the fit of $\tilde{\epsilon}(\omega)$ at 15 K.

To locate the frequencies of the LO-phonon modes (ω_{LO}), we plot the loss function $-\mathrm{Im}[1/\tilde{\epsilon}(\omega)]$,[S3–S5] and identify the peaks. From $\tilde{\epsilon}(\omega)$ in Fig. S1A, we obtain $-\mathrm{Im}[1/\tilde{\epsilon}(\omega)]$ (red circles) in Fig. S1B, thereby identifying one LO-mode frequency at 1.15 THz.

From the fitting parameters [to the dielectric function $\tilde{\epsilon}(\omega)$], we plot $-\mathrm{Im}[1/\tilde{\epsilon}(\omega)]$ and extrapolate to higher frequencies (see solid line Fig. S1B), revealing two Lorentz oscillators,

$$-\mathrm{Im}\left[\frac{1}{\tilde{\epsilon}(\omega)}\right] = \frac{1}{\epsilon_\infty} + \sum_{j=1}^{2} \frac{W_{LO,j}^2}{\omega_{LO,j}^2 - \omega^2 - i\omega\gamma_{LO,j}}, \tag{S3}$$

where $W_{LO,j}^2$, $\omega_{LO,j}$ and $\gamma_{LO,j}$ are the weight, LO-phonon frequency and linewidth of the j^{th}-LO mode, respectively. By fitting $-\mathrm{Im}[1/\tilde{\epsilon}(\omega)]$ to Eq. S3 we obtain the two LO-mode frequencies to be $\frac{\omega_{LO,1}}{2\pi}$ = 1.15 THz (4.8 meV) and $\frac{\omega_{LO,2}}{2\pi}$ = 3.57 THz (14.8 meV). This method was employed in Ref.[S3] for the $CH_3NH_3PbBr_3$ perovskite thin film.

The uncertainty in the value of ΔL leads to error bars in the LO-phonon mode frequencies.[S3] We measured ΔL at 5 positions around the center of the substrates using a Mitutoyo

Table S1: Measurements of z-cut quartz thickness. Abbreviations "Ref." and "Sam." represent the reference substrate, and the substrate where the FCPIB film was deposited, respectively. All measured values in this table are in μm.

Micrometer resolution		Position 1	2	3	4	5	Mean values	Standard errors	ΔL (μm)
0.1 μm	Ref.	1005.1	1005.2	1005.6	1005.1	1004.9	1005.2	0.1	21.5±0.6
	Sam.	984.1	984.7	982.4	982.6	984.9	983.7	0.5	

micrometer with ± 0.1 μm resolution. We calculated the standard deviation of ΔL using these measured thicknesses (see Table S1) to obtain $\Delta L = (21.5 \pm 0.6)$ μm. Within this range of ΔL, $\omega_{LO,1}/2\pi$ ranges within 1.13–1.18 THz, and $\omega_{LO,2}/2\pi$ ranges within 3.00–5.25 THz. Note that, though $\omega_{LO,2}$ differs significantly depending on the value of ΔL, it does not change the conclusions of our paper.

S2. Consistency with the Cochran-Cowley relation

While TO phonon modes are naturally sensitive to THz electromagnetic waves, carries predominantly couple to LO phonons. However, according to the Cochran-Cowley relation,[S6]

$$\frac{\epsilon_{static}}{\epsilon_{\infty}} = \prod_{l=1}^{2} \frac{\omega_{LO,l}^2}{\omega_{TO,l}^2}, \tag{S4}$$

we know that TO and LO modes are interrelated. Therefore, by observing the photoinduced change in the TO mode profiles (Fig. 1C,D), we are indirectly tracking the response of the LO modes.

We now check whether these two LO-phonon frequencies obtained in Section S1 are consistent with the Cochran-Cowley relation. Taking ϵ_{static} ~50 (see Fig. S1A), $\epsilon_{\infty} = 6.8$, the two TO-phonon mode frequencies $\frac{\omega_{TO,1}}{2\pi} = 0.88$ THz and $\frac{\omega_{TO,2}}{2\pi} = 1.76$ THz from our dielectric function data, and $\frac{\omega_{LO,1}}{2\pi} = 1.15$ THz, we calculate $\frac{\omega_{LO,2}}{2\pi}$ to be 3.65 THz — this value of $\frac{\omega_{LO,2}}{2\pi}$ is in excellent agreement with the value of 3.57 THz obtained from our method described in Section S1, hence giving an independent confirmation of the accuracy of the two LO mode frequencies (especially the larger one outside the experimental frequency window).

S3. Carrier–phonon coupling constant calculation

According to Hellwarth *et al.*,[S7] in the presence of multiple scattering channels due to different LO phonon modes, one calculates the effective LO mode frequency ($\omega_{LO,eff}$) from the relations:

$$\frac{W_{LO,eff}^2}{\omega_{LO,eff}^2} = \sum_j \frac{W_{LO,j}^2}{\omega_{LO,j}^2}, \tag{S5}$$

and

$$W_{LO,eff}^2 = \sum_j W_{LO,j}^2, \tag{S6}$$

where $W_{LO,eff}^2$ is the effective weight from all these modes. From Eq. S5 and S6 we obtain

$$\omega_{LO,eff}^2 = \sum_j W_{LO,j}^2 / \sum_j \left(\frac{W_{LO,j}^2}{\omega_{LO,j}^2} \right). \tag{S7}$$

Finally we obtain $\omega_{LO,eff} = 3.45$ THz.

The carrier-phonon coupling constant α are calculated via[S8]

$$\alpha = \sqrt{\frac{m^* e^4}{2\hbar^2 \epsilon_*^2 E_{LO,eff}}}, \tag{S8}$$

where e is the elementary charge, m^* is the band effective mass of the electrons or holes, m_0 is the bare electron mass, $1/\epsilon_* = 1/\epsilon_\infty - 1/\epsilon_{static}$ and $E_{LO,eff} = \hbar\omega_{LO,eff}$. By taking $m_e^* = 0.18m_0$ and $m_h^* = 0.23m_0$ from Ref.,[S9] we calculate the carrier–phonon coupling constant for electrons and holes to be $\alpha_{e-ph} = 1.63$ and $\alpha_{h-ph} = 1.85$, respectively. The polaron mass of electrons and holes are calculated via $m^{**} = (1 + \alpha/6 + 0.0236\alpha^2)$.[S8] Finally we obtain $m_e^{**} = 0.24m_0$ and $m_h^{**} = 0.32m_0$. We use the value of m_e^{**} to calculate the carrier densities in the main text.

S4. J-V characteristics

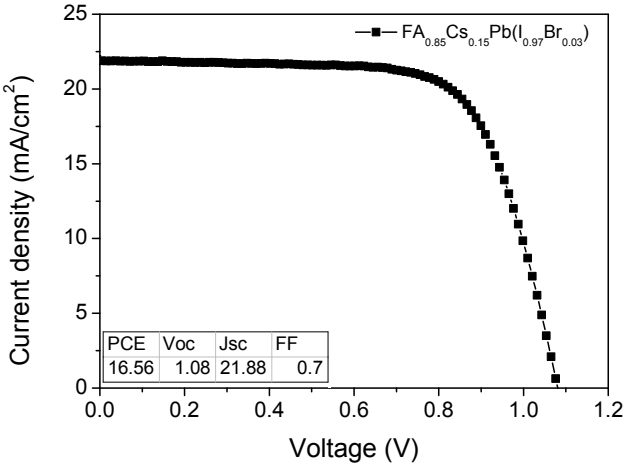

Figure S2: **Current density-voltage (J-V) characteristics on a FCPIB-based solar cell.**

To further characterize the sample, we performed current density-voltage (J-V) characteristics on a FCPIB-based device, as shown in Fig. S2. The PCE is 16.6%, which is considered a high-efficiency solar cell. The J-V characteristics was measured using a calibrated solar simulator (AAA, SAN-EI ELECTRIC CO.,LTD.) coupled with Keithley 2400 Sourcemeter.

Device fabrication: Perovskite solar cell was prepared on pre-cleaned patterned ITO substrate. Poly-TPD was spin-coated from solution (6 mg/mL in chlorobenzene) at 4000 rpm for 40 s, following by baking at 120℃ for 20 min. Prior to the perovskite coating, the poly-TPD surface was treated in UV-ozone cleaner for 10 s. The perovskite precursor solution was spin-coated onto poly-TPD at 1000 rpm for 10 s and 4000 rpm for 30 s, 250 μL chlorobenzene was dripped on the sample surface at 15 s of the second step spin-coating. Subsequently, the perovskite layer was annealed at 80℃ for 5 min, 120℃ for 5 min and 180℃ for 30 min. The PCBM solution was coated from chlorobenzene solution (20 mg/mL) at 1000 rpm for 60 s. The devices were completed by evaporating BCP (6 nm) and Ag (120 nm) sequentially under high vacuum (1×10^{-6} mbar). The active area was 7 mm^2 as defined by the overlapping between back electrode and ITO.

S5. Scanning electron microscopy

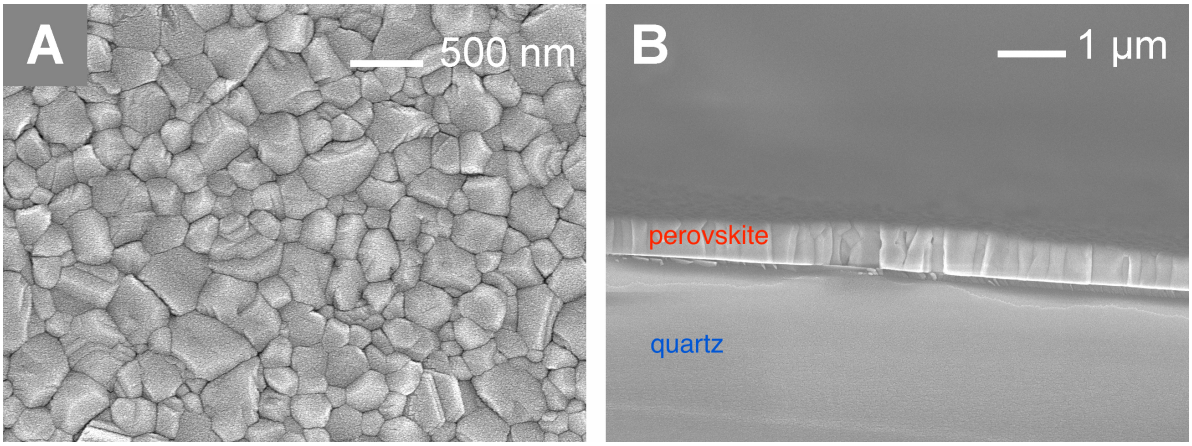

Figure S3: **SEM images of FCPIB thin films on quartz.** SEM images of FCPIB thin films. (A) Top view (B) Cross section.

SEM images were taken on JEOL 7600F. Grain size is about 100–500 nm. The top view and the cross section of perovskite thin films are shown in Fig. S3A and Fig. S3B, respectively.

S6. Absorption spectra

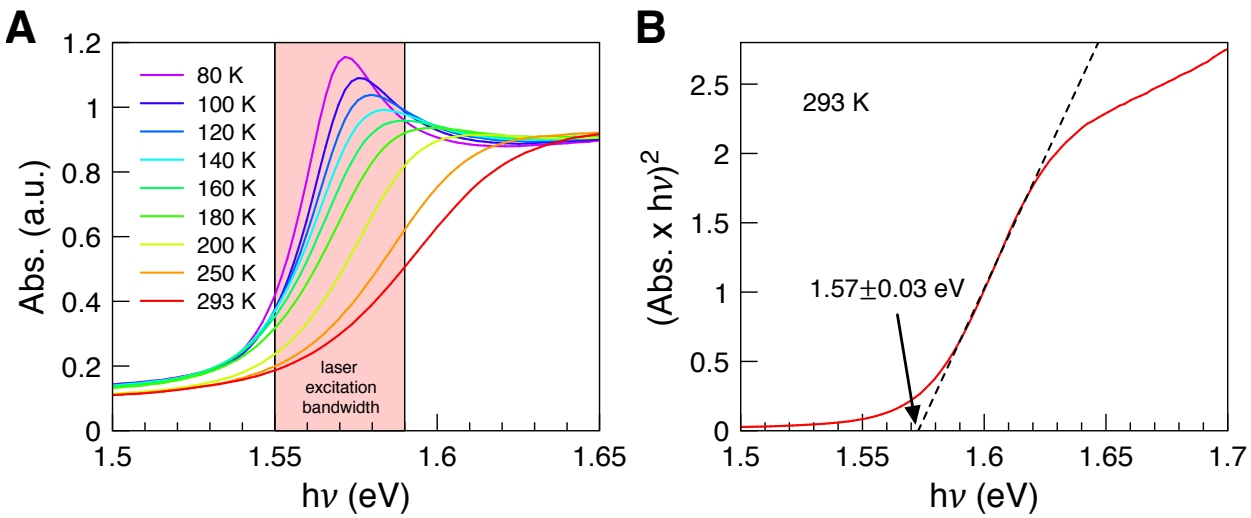

Figure S4: **Absorption spectra.** (A) Temperature-dependent visible absorption spectra. The filled area indicates optical excitation bandwidth. (B) 293 K data (red line). Black dashed line is the fit using Tauc's analysis to obtain the band gap of (1.57 ± 0.03) eV.

We use temperature-dependent steady-state absorption spectra of FCPIB (Fig. S4A) to locate the band gap energy and make sure that the laser wavelength (780 nm to 800 nm) covers the band absorption at all temperatures. By use of Tauc's analysis,[S10] the band gap is estimated at (1.57 ± 0.03) eV (Fig. S4B). The measurement is performed by Varian Cary 100 Bio^{TM} UV-VIS spectrophotometer in a transmission mode.

S7. Photoluminescence

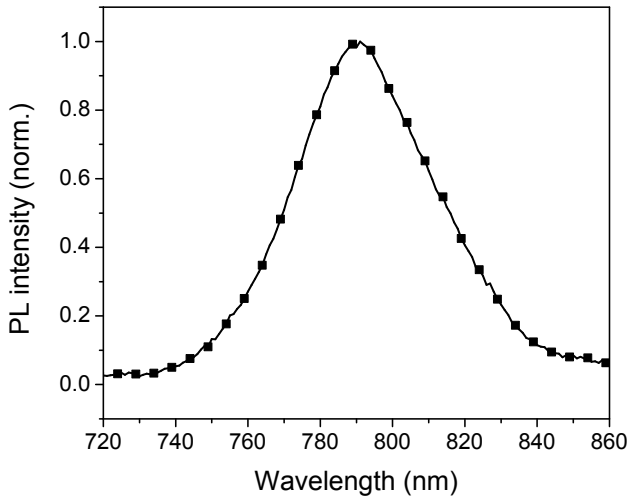

Figure S5: **Photoluminescence spectrum.** Room temperature photoluminescence of FCPIB thin films.

The Photoluminescence spectrum (Fig. S5) was measured by Cary Eclipse fluorescence spectrometer with the excitation wavelength setting on 550 nm and 5-nm slits for both excitation beam and emission beam.

S8. Phonon anharmonicity

In the ideal case where the atoms in a crystal sit in a harmonic potential well of the form

$$U(x) = C_2 x^2, \tag{S9}$$

where $C_2 = k/2$, with k being the force constant and x is the ionic displacement, the oscillator frequency ω is independent of x, given by $\omega = \sqrt{2C_2/m}$, where m is the ionic mass. In the presence of phonon anharmonicity, as has been predicted for the halide perovskites from DFT calculations,[S11] the potential well acquires higher-order terms:

$$U(x) = C_2 x^2 + C_3 x^3 + C_4 x^4 + ... \tag{S10}$$

In this case, the oscillator frequency ω is now a function of x, given by

$$\omega^2(x) = (2C_2 + 3C_3 x + 4C_4 x^2 + ...)/m. \tag{S11}$$

For small values of x, the higher-order terms are negligible. In the perovskites, the absorption of a photon results in large-amplitude vibrations of the lattice,[S12] hence the effects of phonon anharmonicity is large in this class of materials.

S9. Frequency-integrated TRTS

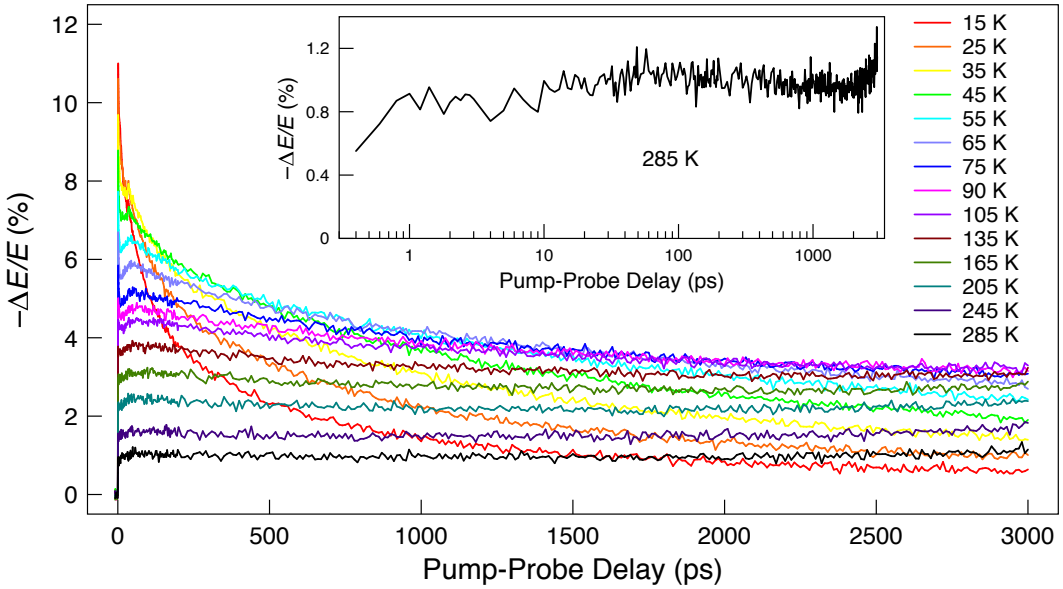

Figure S6: **Frequency-integrated TRTS.** Temperature dependent frequency-integrated TRTS. Inset: 285 K data with pump-probe delay in logarithmic scale.

Figure S6 shows frequency-integrated TRTS data of the FCPIB sample from 15 K to 285 K. The quantity ΔE represents the photoinduced change in the peak of the THz time-domain signal, and $-\Delta E/E$ is proportional to the frequency-averaged photoconductivity $\Delta\sigma$, which, for a constant (time-independent) mobility, gives a measure of the photogenerated carrier density n. Our data shows that at low temperatures, $-\Delta E/E$ decreases with increasing time delay. However, as we approach room temperature, $-\Delta E/E$ starts to display a slow increase, in agreement with the behavior of n shown in Fig. 4A of the main text.

S10. The combined photoconductivity model from phonon and carriers

The THz conductivity in equilibrium due to phonon absorption is usually fitted by a sum of Lorentzian oscillator functions:

$$\tilde{\sigma}_L(\omega) = \sum_{k=1,2} \frac{\epsilon_0 \omega_{pk}^2 \omega}{i(\omega_k^2 - \omega^2) + \omega\gamma_k} - i\epsilon_0\omega(\epsilon_\infty - 1), \tag{S12}$$

where ω_{pk}^2 is proportional to the phonon spectral weight (a measure of the phonon oscillator strength), ω_k is the phonon mode resonance frequency, and γ_k the damping rate of the k^{th} phonon mode, and ϵ_∞ is background dielectric constant. The index k runs up to two to account for two lowest-lying phonon modes in our sample.

If the perturbation to the phonon resonance profile is allowed, the resultant photoinduced change can be written as a first-order differential to the Lorentzian function:

$$\Delta\tilde{\sigma}_L(\omega) = \frac{\partial\tilde{\sigma}_L}{\partial\omega_{pk}^2}\Delta\omega_{pk}^2 + \frac{\partial\tilde{\sigma}_L}{\partial\omega_k}\Delta\omega_k + \frac{\partial\tilde{\sigma}_L}{\partial\gamma_k}\Delta\gamma_k. \tag{S13}$$

By carrying out a straight-forward differentiation and assuming that the damping rate is a constant (from phenomenological observation of our data), we can derive the expression for photoconductivity due to the modified phonon resonances:

$$\Delta\tilde{\sigma}_{PS} = \sum_{k=1,2} \left\{ \frac{\epsilon_0\omega}{i(\omega_k^2 - \omega) + \omega\gamma_k}\Delta\omega_{pk}^2 + \frac{-2i\omega_k\epsilon_0\omega_{p,k}^2\omega}{[i(\omega_k^2 - \omega^2) + \omega\gamma_k]^2}\Delta\omega_k \right\} - i\epsilon_0\omega\Delta\epsilon_\infty. \tag{S14}$$

This 'Peak-Shift' model (PS) contains three free parameters: the phonon spectral weight change $\Delta\omega_{p,k}^2$, phonon frequency shift $\Delta\omega_k$, and the change in background dielectric constant $\Delta\epsilon_\infty$. The rest of the parameters were previously obtained from a separate Lorentzian fit to the phonon modes at equilibrium.

We plot the simulations in Figure S7, under three cases: (A) changes in phonon oscillator

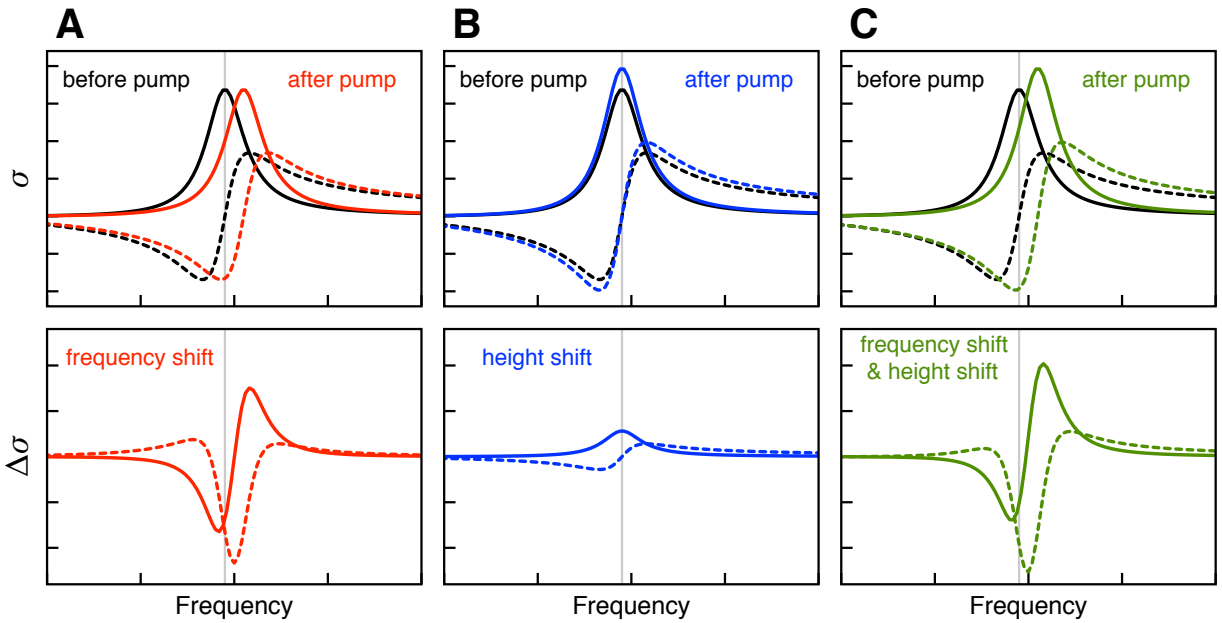

Figure S7: **Simulations of Peak-Shift model.** (A) change in phonon oscillator strength only, (B) change in phonon frequency only and (C) change in both oscillator strength and resonant frequency. Upper figures: THz conductivities before/after pumping the sample. Lower figures: Photoinduced change in these conductivities. Grey vertical lines indicate the phonon frequency before pump. The real and imaginary parts are plotted as solid and dashed curves, respectively.

strength only, (B) changes in phonon frequency only and (C) changes in both oscillator strength and resonant frequency. In case (C), we can see that this PS model is sensitive to both changes in oscillator strength and phonon frequency but is able to extract individual contribution independently, which ensures its reliability.

The PS model can only account for the phonon contribution, but not for the full photoconductivity observed in FCPIB. We have to consider the contribution from the free carriers. As in our previous TRTS work on $MAPbI_3$, we employ the Drude-Smith (DS) model to describe the free-carrier signal in a disordered background:

$$\Delta\tilde{\sigma}_{DS} = \frac{\epsilon_0\omega_{pD}^2}{\gamma_D - i\omega}\left(1 + \frac{c_1}{1 - \frac{i\omega}{\gamma_D}}\right). \tag{S15}$$

The DS model contains three parameters: (1) Drude plasma frequency $\omega_{pD} = \sqrt{\frac{ne^2}{\epsilon_0 m^{**}}}$, where n is the carrier density and m^{**} is the carrier polaronic mass, (2) Drude scattering rate

γ_D which is related to the carrier mobility *via* the relation $\mu = \frac{e}{m^{**}\gamma_D}$, and (3) the parameter c_1 (where $-1 < c_1 < 0$), accounting for backscattering due to sample disorder.

The final combined model is

$$\Delta\tilde{\sigma}(\omega, \tau) = \Delta\tilde{\sigma}_{PS} + \Delta\tilde{\sigma}_{DS}. \tag{S16}$$

S11. Temperature-dependent THz conductivities of thin-film FCPIB

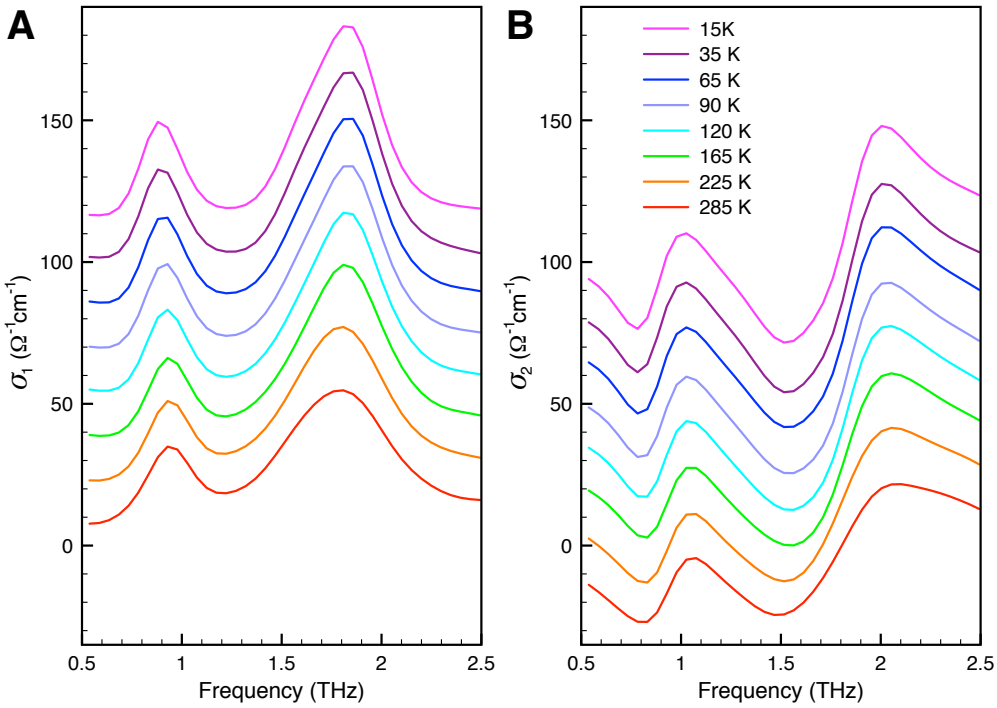

Figure S8: **Temperature-dependent THz conductivities of thin-film FCPIB.** (A) real part $\sigma_1(\omega)$ and (B) imaginary part $\sigma_2(\omega)$. The data are offset vertically.

We performed temperature-dependent THz-TDS measurements on FCPIB. Figure S8 shows the optical conductivities as a function of lattice temperature. We see there are only two phonon modes in the frequency range of 0.5–2.5 THz, which is consistent with our previous works, due to the similar Pb-halide bond vibrations.[S3,S13] The phonon mode frequency changes very little with temperature. No phonon mode splitting is observed in the temperature range of 15–285 K.

References

(S1) Zou, X.; Shang, J.; Leaw, J.; Luo, Z.; Luo, L.; La-o-vorakiat, C.; Cheng, L.; Cheong, S. A.; Su, H.; Zhu, J.-X.; Liu, Y.; Loh, K. P.; Castro Neto, A. H.; Yu, T.; Chia, E. E. M. Terahertz Conductivity of Twisted Bilayer Graphene. *Phys. Rev. Lett.* **2013**, *110*, 067401.

(S2) La-o-vorakiat, C.; Cheng, L.; Salim, T.; Marcus, R. A.; Michel-Beyerle, M.-E.; Lam, Y. M.; Chia, E. E. M. Phonon Features in Terahertz Photoconductivity Spectra Due to Data Analysis Artifact: A Case Study on Organometallic Halide Perovskites. *Appl. Phys. Lett.* **2017**, *110*, 123901.

(S3) Zhao, D.; Skelton, J. M.; Hu, H.; La-o-vorakiat, C.; Zhu, J.-X.; Marcus, R. A.; Michel-Beyerle, M.-E.; Lam, Y. M.; Walsh, A.; Chia, E. E. M. Low-Frequency Optical Phonon Modes and Carrier Mobility in the Halide Perovskite $CH_3NH_3PbBr_3$ Using Terahertz Time-Domain Spectroscopy. *Appl. Phys. Lett.* **2017**, *111*, 201903.

(S4) Lowndes, R. P. Influence of Lattice Anharmonicity on the Longitudinal Optic Modes of Cubic Ionic Solids. *Phys. Rev. B* **1970**, *1*, 2754–2763.

(S5) Huber, R.; Kübler, C.; Tübel, S.; Leitenstorfer, A.; Vu, Q. T.; Haug, H.; Köhler, F.; Amann, M.-C. Femtosecond Formation of Coupled Phonon-Plasmon Modes in InP: Ultrabroadband THz Experiment and Quantum Kinetic Theory. *Phys. Rev. Lett.* **2005**, *94*, 027401.

(S6) Cochran, W.; Cowley, R. A. Dielectric Constants and Lattice Vibrations. *J. Phys. Chem. Solids.* **1962**, *23*, 447–450.

(S7) Hellwarth, R. W.; Biaggio, I. Mobility of an Electron in a Multimode Polar Lattice. *Phys. Rev. B* **1999**, *60*, 299.

(S8) Feynman, R. P. Slow Electrons in a Polar Crystal. *Phys. Rev.* **1955**, *97*, 660.

(S9) Amat, A.; Mosconi, E.; Ronca, E.; Quarti, C.; Umari, P.; Nazeeruddin, M. K.; Grätzel, M.; De Angelis, F. Cation-Induced Band-Gap Tuning in Organohalide Perovskites: Interplay of Spin–Orbit Coupling and Octahedra Tilting. *Nano Lett.* **2014**, *14*, 3608–3616.

(S10) Kasap, S., Capper, P., Eds. *Springer Handbook of Electronic and Photonic Materials*; Springer: New York, 2017.

(S11) Whalley, L. D.; Skelton, J. M.; Frost, J. M.; Walsh, A. Phonon Anharmonicity, Lifetimes, and Thermal Transport in $CH_3NH_3PbI_3$ from Many-Body Perturbation Theory. *Phys. Rev. B* **2016**, *94*, 220301.

(S12) Wu, X.; Tan, L. Z.; Shen, X.; Hu, T.; Miyata, K.; Trinh, M. T.; Li, R.; Coffee, R.; Liu, S.; Egger, D. A.; Makasyuk, I.; Zheng, Q.; Fry, A.; Robinson, J. S.; Smith, M. D.; Guzelturk, B.; Karunadasa, H. I.; Wang, X.; Zhu, X.; Kronik, L. *et al.* Light-Induced Picosecond Rotational Disordering of the Inorganic Sublattice in Hybrid Perovskites. *Sci. Adv.* **2017**, *3*, e1602388.

(S13) La-o-vorakiat, C.; Xia, H.; Kadro, J.; Salim, T.; Zhao, D.; Ahmed, T.; Lam, Y. M.; Zhu, J.-X.; Marcus, R. A.; Michel-Beyerle, M.-E.; Chia, E. E. M. Phonon Mode Transformation Across the Orthohombic–Tetragonal Phase Transition in a Lead Iodide Perovskite $CH_3NH_3PbI_3$: A Terahertz Time-Domain Spectroscopy Approach. *J. Phys. Chem. Lett.* **2016**, *7*, 1–6.